








# QRS-T Angles as Markers for Heart Sphericity in Subjects With Intrauterine Growth Restriction: A Simulation Study

Freddy L. Bueno-Palomeque , Member, IEEE, Konstantinos A. Mountris , Nuria Ortigosa , Raquel Bailón , Member, IEEE, Bart Bijmens , Fátima Crispi , Esther Pueyo , Ana Mincholé , and Pablo Laguna , Fellow, IEEE

**Abstract**—Changes induced by intrauterine growth restriction (IUGR) in cardiovascular anatomy and function that persist throughout life have been associated with a higher predisposition to heart disease in adulthood. Together with cardiac morphological remodelling, evaluated through the ventricular sphericity index, alterations in cardiac electrical function have been reported by characterization of the depolarization and repolarization loops, and their angular relationship, measured from the vectorcardiogram. The underlying relationship between the morphological remodelling and the angular variation of QRS and T-wave dominant vectors, if any, has not been explored. The aim of this study was to evaluate this relationship using computational models based on realistic heart and torso in which IUGR-induced morphological changes were incorporated by reducing the ventricular sphericity index. Specifically, we departed from a control model and we built

eight different globular heart models by reducing the base-to-apex length and enlarging the basal ventricular diameter. We computed QRS and T-wave dominant vectors and angles from simulated pseudo-electrocardiograms and we compared them with clinical measurements. Results for the QRS to T angles follow a change trend congruent with that reported in clinical data, supporting the hypothesis that the IUGR-induced morphological remodelling could contribute to explain the observed angle changes in IUGR patients. By additionally varying the position of the ventricles with respect to the torso and the electrodes, we found that electrode displacement can impact the quantified angles and should be considered when interpreting the results.

**Index Terms**—Intrauterine growth restriction, cardiac remodelling, globular heart, sphericity index, electrocardiogram.

Manuscript received 20 March 2023; revised 16 June 2023; accepted 17 July 2023. Date of publication 21 July 2023; date of current version 5 October 2023. This work was supported in part by Fundación Carolina and Universidad Politécnica Salesiana, in part by the Spanish Ministry of Science and Innovation (MICINN) and FEDER Una manera de hacer Europa under Grants PID2019-105674RB-I00, PID2021-128972OA-I00, TED2021-130459B-I00, and PID2020-119457GB-I00, through Ramon y Cajal Program under Grant RYC2019-027420-I, in part by the Gobierno de Aragón, Reference Group BSICoS T39-20R, and in part by Project LMP94\_21. (Corresponding author: Freddy L. Bueno-Palomeque.)

Freddy L. Bueno-Palomeque is with the GIHEA, Universidad Politécnica Salesiana, Cuenca 010102, Ecuador, and also with the BSI-CoS Group, I3A, IIS Aragón, CIBER en Bioingeniería, Biomateriales y Nanomedicina, Universidad de Zaragoza, 50018 Zaragoza, Spain (e-mail: fbueno@ups.edu.es).

Konstantinos A. Mountris is with the Mechanical Engineering, University College London, WC1E 6BT London, U.K. (e-mail: konstantinos.mountris@gmail.com).

Nuria Ortigosa is with the I.U. Matemática Pura y Aplicada, Universitat Politècnica de València, 46022 Valencia, Spain (e-mail: nuorar@upvnet.upv.es).

Raquel Bailón, Esther Pueyo, Ana Mincholé, and Pablo Laguna are with the BSICoS Group, I3A, IIS Aragón, CIBER en Bioingeniería, Biomateriales y Nanomedicina, Universidad de Zaragoza, 50018 Zaragoza, Spain (e-mail: rbailon@unizar.es; epueyo@unizar.es; mincholé@unizar.es; laguna@unizar.es).

Bart Bijmens is with the ICREA, Institut d'Investigacions Biomèdiques August Pi i Sunyer (IDIBAPS), 46022 Barcelona, Spain (e-mail: bart.bijmens@upf.edu).

Fátima Crispi is with the BCNatal - Barcelona Center for Maternal-Fetal and Neonatal Medicine, Hospital Sant Joan de Déu and Hospital Clínic, University of Barcelona, 08007 Barcelona, Spain (e-mail: fcrispi@clinic.cat).

Digital Object Identifier 10.1109/JBHI.2023.3297550

## I. INTRODUCTION

**I**NTRAUTERINE growth restriction (IUGR) defined as impaired fetal growth during pregnancy, has been associated with higher risk of cardiovascular mortality and stroke throughout adulthood [1]. IUGR is an important obstetric condition affecting 7–10% of fetuses in their mother's womb during pregnancy, with an importantly higher incidence in underdeveloped/developing countries as compared to developed countries [2]. IUGR subjects undergo structural and functional cardiovascular changes in the fetal stage that persist in the postnatal life through infancy, childhood, and adolescence, and could explain the increased predisposition to cardiovascular disease in adult life.

Cardiac structural remodelling has been reported to occur in the fetal stage and continues into infancy (six months corrected age), showing more globular heart, thicker myocardial walls, reduced longitudinal motion, and impaired relaxation with increased radial function [3], [4]. Similar features have been found in a cohort of IUGR preadolescents [5] with larger basal diameter reducing the sphericity index and a shortening of the apicobasal distance resulting in reduced longitudinal movement in the ventricles confirmed by 2D, 3D echocardiography and blood pressure measurements. Persistence of these changes in adulthood is however controversial [6], [7].

In parallel to the described structural remodelling, alterations in cardiac electrical function have been reported

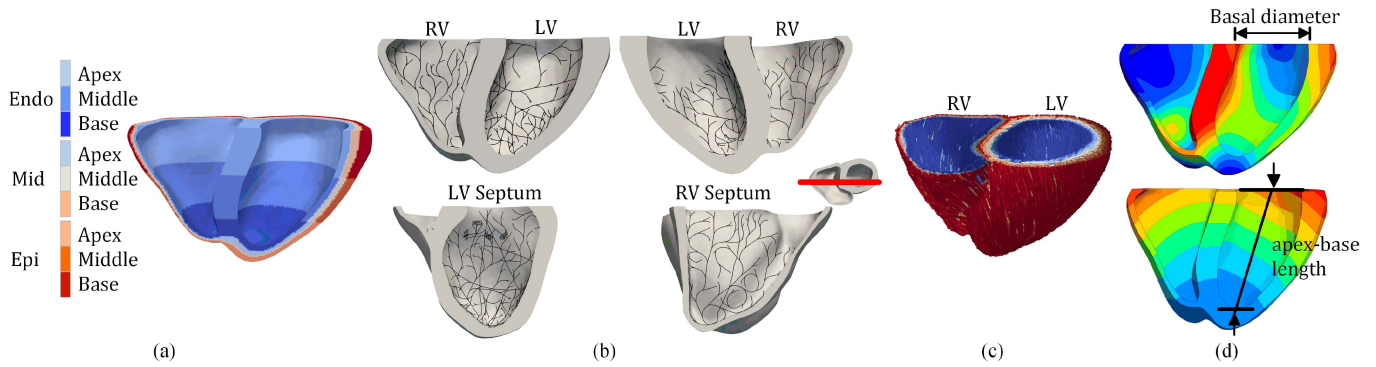


**Fig. 1.** Parameters considered on the  $\mathcal{C}$  and  $\mathcal{G}$  models. (a) Mesh segmentation considering transmural (endo/mid/epi myocardium) and gradient heterogeneities (apex/intermediate/base, dark blue to light blue), (b) Purkinje network on the endocardial surface, (c) fiber orientation from endocardial (blue lines) to epicardial surface (red lines), and (d) color map showing the nodal displacement on the  $\mathcal{C}$  model to obtain the  $\mathcal{G}$  models.

in preadolescents with IUGR by evaluating changes in the dominant depolarization and repolarization angular relationship with respect to the three spatial planes as measured by the vectorcardiogram (VCG). Wider angles between dominant QRS and T-wave vectors [8] and larger QRS angles in the XY plane [9] compared to controls were identified using 12-lead electrocardiographic (ECG) signals. Wider QRS-T angles representing larger depolarization-repolarization differences have been shown to be predictive of ventricular arrhythmias in other patient populations [10]. The reported changes in cardiac electrical activity in preadolescents with IUGR could help to explain their predisposition to cardiovascular disease in adulthood. As the ECG is largely influenced by anatomical features, it is worth to investigate whether the IUGR-associated cardiac structural remodelling is responsible for some of the observed differences in the electrophysiological function in IUGR subjects. To address this question, multiscale computational models of the human heart integrating both anatomical and electrophysiological information have been used in this study. The aim is to quantify the effect of the anatomical cardiac remodelling in IUGR subjects on the angular relationships of the dominant depolarization and repolarization VCG angles. Simulation results were compared with clinical findings on IUGR-induced changes in QRS-to-T angle changes [9], allowing to shed light on the contributions of structural and functional remodelling to ECG abnormalities in IUGR subjects. In addition, the role of inter-subject variability in the obtained results is assessed. Preliminary results were presented in a conference [11].

## II. MATERIALS AND METHODS

### A. Computational Model of Human Electrophysiology

*In silico* simulations of the QRS and T-wave loops were conducted using a biventricular geometry [12], taken as the reference model. The geometry was meshed using tetrahedral elements (1872709 elements and 345870 nodes). We used the software ELECTRA [13], which implements the finite element method to solve the monodomain model of electrical propagation in cardiac tissue, to conduct the numerical simulations of the study.

The electrical propagation started at the bundle of His and propagated through the Purkinje network until reaching the endocardial tissue. The Purkinje network was implemented in the model using a method based on fractal projection [14] (Fig. 1(b)). The different anisotropic conductivities in the ventricular myocardium and the His-Purkinje were adjusted using appropriate diffusion coefficients and set to result in a longitudinal conduction velocity of 67 cm/s in the myocardium and of 2.5–3.0 m/s in the His-Purkinje system, respectively [15]. The cellular membrane kinetics of the Purkinje network was represented by the Stewart action potential (AP) model [15] and the human ventricular cell electrophysiology by the O’Hara-Rudy AP model for healthy tissue [16].

Electrophysiological propagation was simulated by incorporating a fiber architecture using a rule-based method [17], following the Streeter rule from apex to base in a counterclockwise direction, from  $-60^\circ$  on the endocardium to  $60^\circ$  on epicardium tissue on the two ventricles [18] (Fig. 1(c)). A sequence of three stimuli, separated by 1000 ms, was applied to generate the electrical activity in the ventricles. The stimuli consisted of a squared impulse with amplitude of 200 mA and duration of 0.5 ms. The third beat was used for analysis.

The voltage in the biventricular mesh and in the torso volume where it was embedded were used to compute extracellular potentials, using a monodomain cell model. Virtual electrodes were positioned on the torso surface at standard electrode positions to compute the 12-lead ECG [19]. To assess the dominant vector direction of the electrical wavefront along the depolarization and repolarization loops, we used the inverse Dower’s transform [20] to transform the 12-lead ECG into the orthogonal leads X, Y, and Z of a VCG, rather than directly computing the VCG. The rationale behind this is to closely replicate the approach used in the studies analyzing clinical data [8], which are being used as a reference for comparing the results. Next, we calculated the angles of the dominant vectors relative to the transverse, XZ, frontal, XY, and sagittal, ZY planes according to the angular variables measured in [9].

The projection of the QRS-T angle on the XY plane was calculated ( $\theta_{RT-XY}$ ). Three angles were determined between the QRS loop vector and each of the three VCG planes ( $\phi_{R-XZ}$ ,

$\phi_{R-XY}$ , and  $\phi_{R-ZY}$ ), and other three for the T-wave vector ( $\phi_{T-XZ}$ ,  $\phi_{T-XY}$ , and  $\phi_{T-ZY}$ ). Finally, the angular difference between the QRS and T-Wave on each of the three planes was calculated ( $\phi_{R-XZ} - \phi_{T-XZ}$ ,  $\phi_{R-XY} - \phi_{T-XY}$ , and  $\phi_{R-ZY} - \phi_{T-ZY}$ ).

Three different stages were simulated for evaluation of the angular variables. First, simulations were performed in the control model ( $\mathcal{C}$ ) incorporating transmural and apicobasal heterogeneities, as described in Section II-B. Second, the control model was deformed to make the ventricles more globular ( $\mathcal{G}$ ) using eight different strategies,  $\mathcal{G}_A$  to  $\mathcal{G}_H$ . Subsequently, different transmural heterogeneities were incorporated in two representative deformed models,  $\mathcal{G}_C$  and  $\mathcal{G}_H$ . In the third stage, a global displacement test applied to the  $\mathcal{C}$  model was introduced by moving all mesh nodes equally.

### B. Transmural and Apicobasal Heterogeneities Modeling Intersubject Variability

Transmural heterogeneities in the membrane kinetics were incorporated by defining different proportions of endocardial, midmyocardial and epicardial cells along the ventricular wall (Fig. 1(a)). A total of fifteen configurations were developed considering variations from 10% to 30%, in steps of 10%, in the midmyocardial, and this paired with all possible combinations from 10% to 50% in the endocardial, and 20% to 80% in the epicardial segment, restricted transmurally to sum up to 100%, see Fig. 4. Each configuration was denoted as  $C_{uvw}$  where  $u$ ,  $v$  and  $w$  denote the first digit of the proportions of endo-, mid- and epicardial cells, respectively,  $u + v + w = 10$ , (e.g. C334 represents the case with 30% endo-, 30% mid- and 40% epicardial cells).

We identified three surfaces on the mesh model, the left and right ventricular endocardial surfaces and the epicardial surface. From the  $k$ -th nodes in the mesh, located at coordinates  $\mathbf{n}_k = [x_k \ y_k \ z_k]$ , we selected those which corresponded to the ventricular endocardial surfaces,  $\mathbf{n}_{k_{en}}$ ,  $k_{en}$  belonging to the subset of  $\{k \in Endo\}$ , and look out for the nearest point in the epicardial surface  $\mathbf{n}_{k_{ep}}$ ,  $k_{ep}$  in the subset  $\{k \in Epi\}$ , by determining the minimal Euclidean distance,  $D_m(k_{en})$ , between two nodes as

$$D_m(k_{en}) = \min_{k_{ep}} \left\| [x_{k_{en}} \ y_{k_{en}} \ z_{k_{en}}] - [x_{k_{ep}} \ y_{k_{ep}} \ z_{k_{ep}}] \right\|. \quad (1)$$

A proportion,  $p_{en}$ , of the nodes in the  $D_m(k_{en})$  transmural section from endo to epi, departing from endo, were set to endocardial nodes. Another proportion,  $p_{ep}$ , of those departing from epicardium were set to epicardial nodes. Those in middle were considered as midmyocardial nodes. This was implemented by considering a sphere with center in  $[x_{k_{en}} \ y_{k_{en}} \ z_{k_{en}}]$  and radius  $p_{en} \times D_m(k_{en})$ . Every node inside the sphere was classified as an endocardial node. This process was repeated for the epicardial nodes. The complete interventricular septum was considered as endocardial cells. Simulations were run for each one of the possible endo/mid/epi combinations. Additionally, apex-to-base electrophysiological heterogeneities were introduced in the model. The model was divided in three segments along the apex-to-base direction: apex, middle, and base. These

were assigned with a factor to multiply and reduced  $I_{Ks}$ . In particular, the conductance  $G_{Ks}$  was varied from 0% at the apex ( $G_{Ks} \times 5.0$ ) to 48% decrease at the middle ( $G_{Ks} \times 2.6$ ) to 96% at the base ( $G_{Ks} \times 0.2$ ) [21] (Fig. 1(a)).

### C. Anatomical Model With Increased Sphericity Index

The changes resulting from cardiac morphological remodeling in IUGR patients were represented by the  $\mathcal{G}$  models, which were built based on the control model  $\mathcal{C}$ . To build  $\mathcal{G}$  from  $\mathcal{C}$ , we incorporated echocardiographic findings on left and right ventricular morphometry as reported in [5]. Specifically, we increased the basal diameter and shortened the apex-base length, resulting in a reduction of the sphericity index (see Table I). In order to focus the study on evaluating the impact of geometrical changes on the simulations, the electrophysiological characteristics of the  $\mathcal{G}$  model, such as fiber orientation, ventricular heterogeneities, and conduction velocity, were kept unchanged as previously described in the control model.

To deform the  $\mathcal{C}$  model, we used the nonlinear finite element solver for biomechanics FEBIO v2.9.1 [22]. The cardiac tissue was modeled as an isotropic, homogeneous, hyperelastic, and incompressible Mooney-Rivlin material [23] with an invariant term  $C1 = 0.38$  MPa and  $C2 = 0.31$  MPa. Nodes,  $\mathbf{n}_k = [x_k \ y_k \ z_k]$  were deformed, generating a nodal displacement to  $\mathbf{n}_k + \mathbf{d}_k$ , with  $\mathbf{d}_k = [u_k \ v_k \ w_k]$ .

We generated eight distinct deformed models  $\mathcal{G}$  with the same sphericity index (Fig. 2). We first applied three different strategies to increase the basal diameter of the control geometry by applying a load on the basal diameter axis:  $\mathbf{d}_k = [0 \ f_y(y_k) \ 0]$ .

- The first strategy, denoted as (Y→), expanded the epicardium of the left ventricle by applying a surface traction on the epicardial surface with a boundary condition  $f_y(y_k) = 0$  for  $y_k$  in the septum, set at no displacement.
- In the second strategy, we applied a similar load on the septal left wall (Y←),  $f_y(y_k) = 0$  for  $y_k$  in the left ventricular wall.
- In the third strategy, a similar load was homogeneously applied to the entire endocardial wall of the left ventricle (Y ↔),  $\mathbf{d}_k = [f_x(x_k) \ f_y(y_k) \ 0]$ ,  $f_x(x_k)$ ,  $f_y(y_k) = 0$  for  $x_k$  and  $y_k$  in the right ventricular wall.

We also applied three different strategies to reduce the apex-to-base length,  $\mathbf{d}_k = [0 \ 0 \ f_z(z_k)]$ .

- In the first strategy, a surface load ( $Z \uparrow$ ) was applied to the apex,  $f_z(z_k) = 0$  for  $z_k$  in the base.
- In the second strategy ( $Z \downarrow$ ), the load was applied to the base, with  $f_z(z_k) = 0$  for  $z_k$  in the apex.
- In the third strategy ( $Z \updownarrow$ ), a scale factor,  $\alpha$ , was introduced to homogeneously reduce the apex-base length,  $L_{AB}$ , up to  $L_{AB} - \Delta L_{AB}$ ,  $\alpha = \Delta L_{AB} / L_{AB}$ . We calculated the displacement on the Z axis as  $f_z(z_k) = \alpha(z_r - z_k)$ , where  $z_r$  is the zero displacement reference coordinate.  $\mathcal{G}_C$  and  $\mathcal{G}_D$  models meet  $f_z(z_r) = 0$  at the apex, and  $\mathcal{G}_H$  and  $\mathcal{G}_D$  models meet  $f_z(z_r) = 0$  at the base (Fig. 2).

The surface loads were applied on each one of the triangle surface elements, resulting in a total displacement



TABLE I  
BASE-APEX LENGTH, BASAL DIAMETER, AND SPHERICITY INDEX DATA FROM ECHOCARDIOGRAPHIC MEASUREMENTS, WITH STATISTICAL DIFFERENCE BETWEEN PATIENT GROUPS, [5] AND THE SAME MORPHOMETRY MEASUREMENTS IN THE SIMULATIONS  $\mathcal{C}$  AND  $\mathcal{G}_A$  TO  $\mathcal{G}_H$  MODELS

		Base-apex length (cm)		Basal diameter (cm)		Sphericity index	
		Left	Right	Left	Right	Left	Right
Clinical data	Control subjects	6.9 ± 0.6	6.5 ± 0.6	3.4 ± 0.3	3.0 ± 0.4	2.0 ± 0.01	2.1 (0.2 - 0.22)
	IUGR subjects	6.4 ± 0.6	6.1 ± 0.6	3.5 ± 0.3	3.0 ± 0.3	1.9 ± 0.01	2.0 (0.1 - 0.2)
	p-value	0.003	0.01	0.003	0.32	<0.001	0.006
Simulation	Control ( $\mathcal{C}$ )	7.0	5.7	4.6	4.2	1.5	1.4
	Deformed ( $\mathcal{G}$ )						
	$\mathcal{G}_A$ [ $Y \leftarrow, Z \uparrow$ ]	6.5	5.3	4.7	4.2	1.4	1.3
	$\mathcal{G}_B$ [ $Y \leftarrow, Z \downarrow$ ]	6.5	5.3	4.7	4.2	1.4	1.3
	$\mathcal{G}_{C, D}$ [ $Y \leftarrow, Z \updownarrow$ ]	6.5	5.3	4.7	4.2	1.4	1.3
	$\mathcal{G}_E$ [ $Y \rightarrow, Z \uparrow$ ]	6.5	5.2	4.7	4.3	1.4	1.2
	$\mathcal{G}_F$ [ $Y \rightarrow, Z \downarrow$ ]	6.5	5.2	4.7	4.3	1.4	1.2
	$\mathcal{G}_{G, H}$ [ $Y \leftrightarrow, Z \updownarrow$ ]	6.5	5.4	4.7	4.2	1.4	1.3

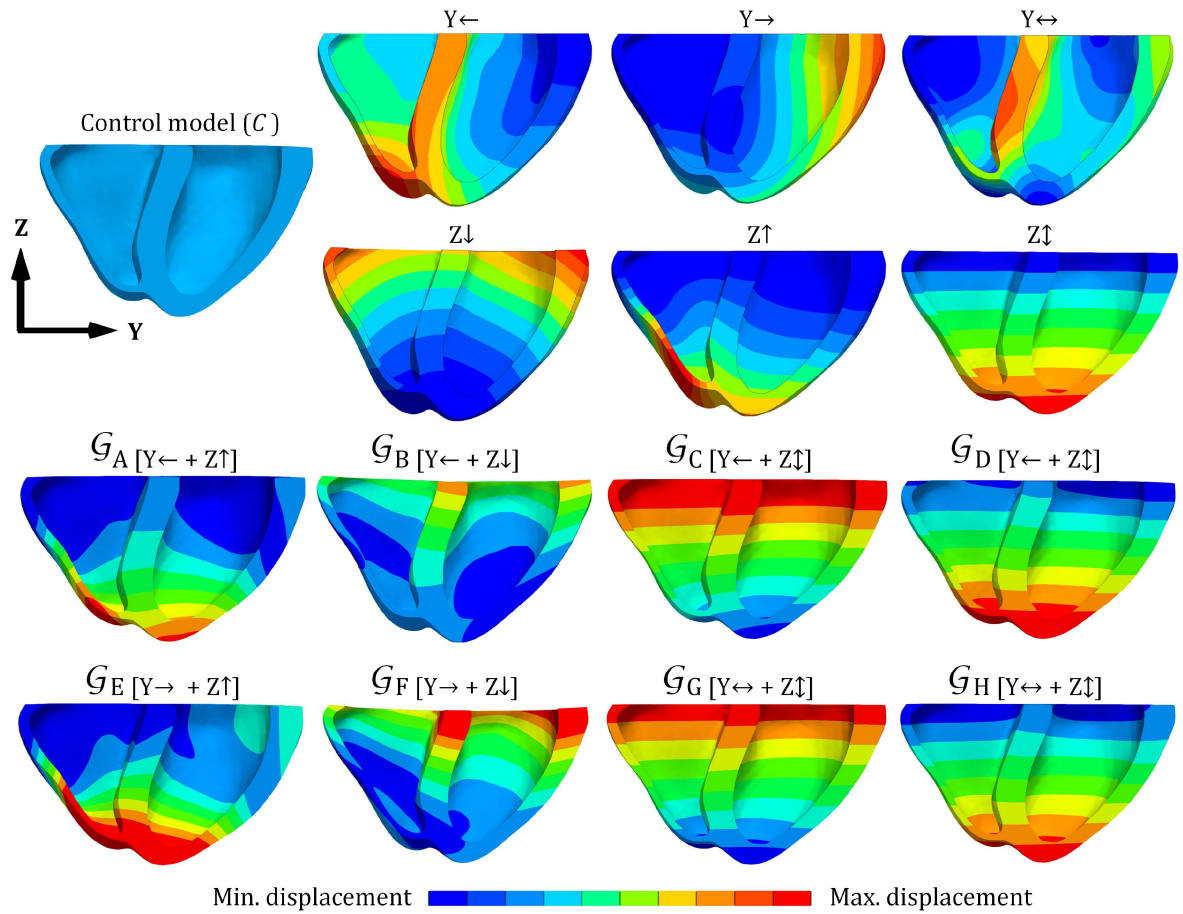


Fig. 2. Upper part shows, through the color map, the nodal displacement obtained as a result of the deformation of the original control model  $\mathcal{C}$ . The Y and Z axes were associated with the deformation in the basal diameter and in the apex-base length, respectively. The eight  $\mathcal{G}$  models resulting from combining the deformations in Y and Z axes were shown at the bottom.

$\mathbf{d}_k = [u_k \ v_k \ w_k]$  formed by the summation of the apex-base and endo-epi displacements, and applied to the original mesh to generate the eight  $\mathcal{G}$  models (Fig. 2). Twelve deformed models were obtained through the combination of the three methods for basal diameter deformation with the four methods for apex-base deformation. Four models were excluded from the study as the

angles of depolarization and repolarization they produced fell outside the physiological limits. This could be attributed to a less uniform distribution of deformation resulting from the combined methods of modifying the basal diameter and apex-base length. Fig. 2 displays the eight models that were retained for analysis.

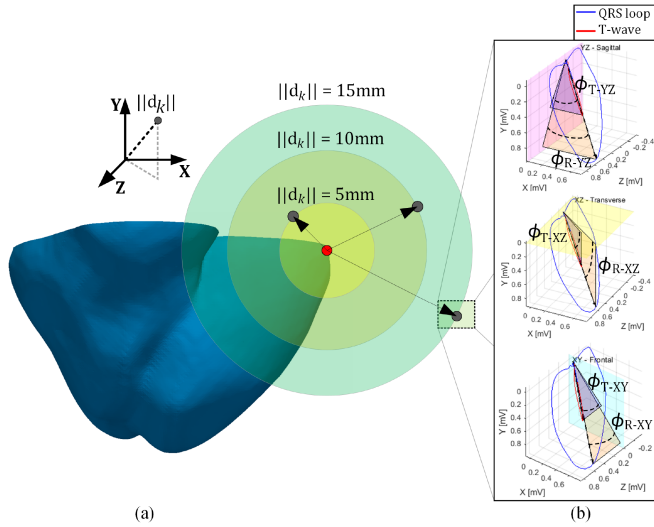


Fig. 3. Displacement tests for  $\mathcal{C}$  model, C334 configuration, when moving by 5, 10, and 15 mm on the mesh. (a) location grid around a red point representing one node of the mesh and its relocation. Each gray point represents the displacement of each of the nodes of the model in any direction. 120  $\mathbf{d}_k$  displacements were made around the original point, at 5, 10, and 15 mm. (b) QRS and T-wave vectors and their angles with respect to the three corporal planes. Note that T-wave (red line) and QRS (blue line) loops have a similar dominant vector direction.

#### D. Confounding Effect of Heart Location Within the Torso

The morphological remodelling that includes a reduction in the sphericity index may be accompanied by a displacement of the heart anatomy within the thoracic cage. Therefore, we investigated the effect on angles estimates of a global displacement of the biventricular  $\mathcal{C}$  model. The model was relocated in the three axis in one hundred and twenty different forms, by displacing each node  $\mathbf{n}_k$  according to the vector  $\mathbf{d}_k = [\Delta x \ \Delta y \ \Delta z]$  where  $\|\mathbf{d}_k\| \in \{5, 10, 15\}$  mm (Fig. 3). The pseudo-ECG was computed considering the displacement of the biventricular model inside the torso mesh and the dominant vectors from the VCG were computed.

### III. RESULTS

#### A. Angular Variation Due to Transmural Heterogeneities

Variability in the depolarization and repolarization VCG and ECG leads was introduced by using different transmural proportions of endo, mid and epi cells across the ventricular wall. The resulting X, Y and Z leads are shown in Fig. 4. Dotted lines show the QRS and T-wave time intervals from which the dominant vectors were computed. The QRS interval expanded from 12 to 85 ms and the T wave from 200 to 378 ms. Fig. 4 shows the variation in the T-wave corresponding to different tissue heterogeneities for the fifteen simulated combinations described in the table of Fig. 4.

The calculated angles of the QRS and T-wave loops with respect to the three corporal planes from different  $C_{uvw}$  configurations were plotted in Fig. 5, leftmost boxplot in each angle column. The angles variance across the  $C_{uvw}$  configurations were: in the frontal plane XY, 2.6°, 3.0°, and 3.7°

		% Endo				% Epi	
		10	20	30	40		50
						<b>C532</b>	20
					C433	C523	30
				<b>C334</b>	C424	C514	40
			C235	C325	C415		50
	<b>C136</b>	<b>C226</b>	<b>C316</b>				60
	<b>C127</b>	<b>C217</b>					70
	<b>C118</b>						80

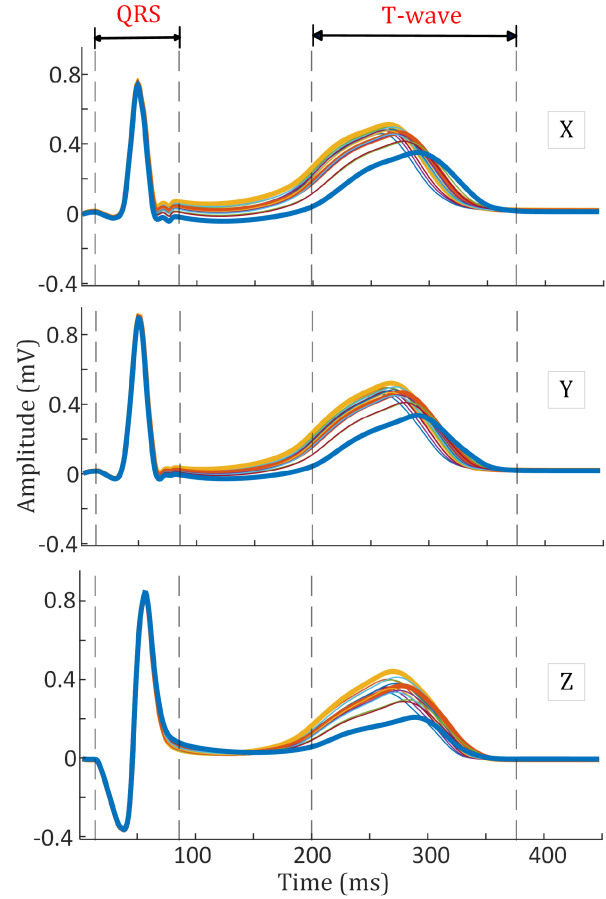
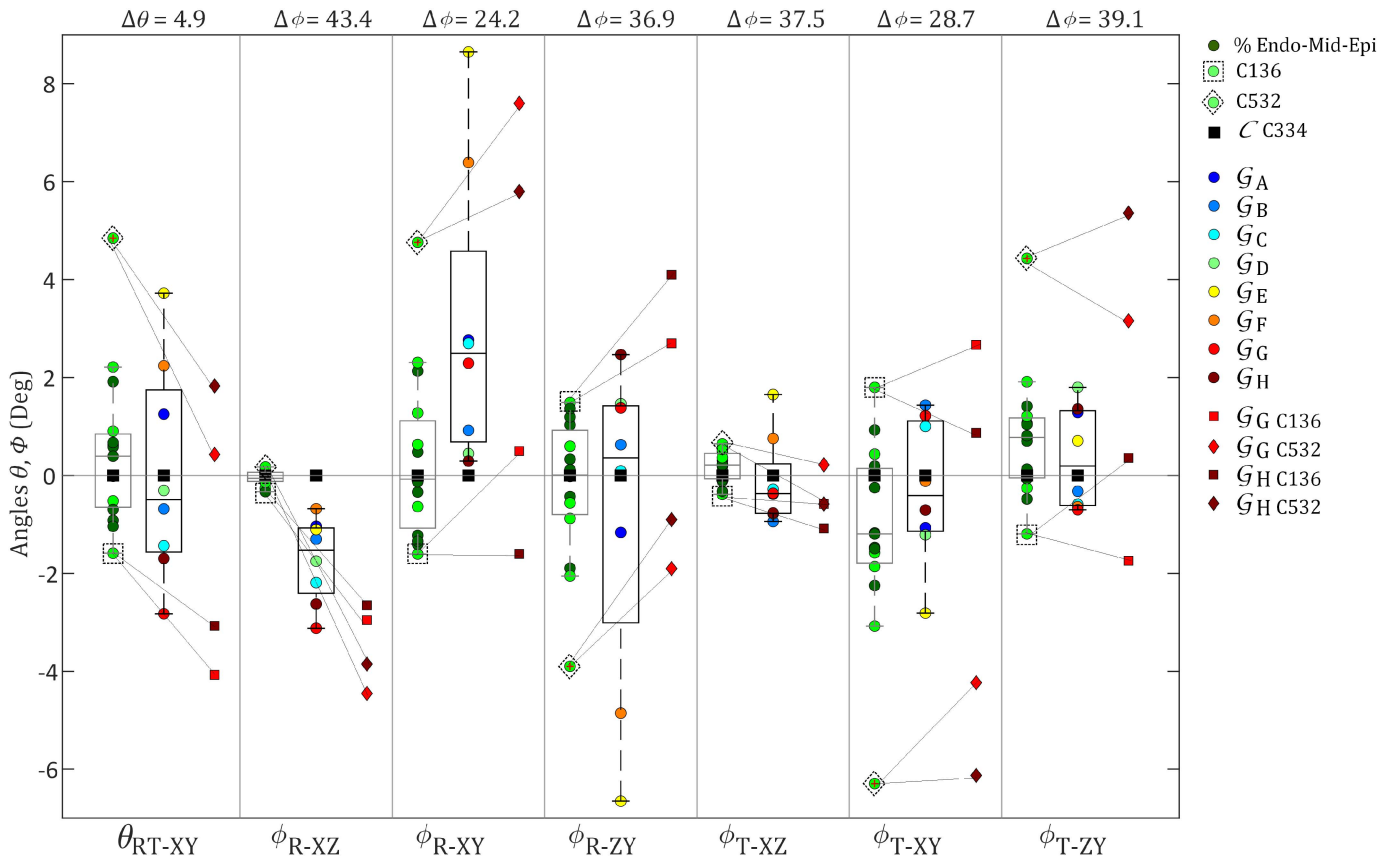


Fig. 4. List of the different transmural tissue heterogeneities configurations. Columns and rows indicate the percentage of endocardium and epicardium respectively. Bold lines correspond to configurations with inter-middle (C334) and extremes (C136 and C532) T-wave amplitudes. X, Y, and Z leads computed using the biventricular model at the  $\mathcal{C}$  case, combining different endo-mid-epi tissue configurations,  $C_{uvw}$ . Dotted lines show QRS and T-wave time intervals from where the dominant vectors were computed.

for  $\theta_{RT-XY}$ ,  $\phi_{R-XY}$ , and  $\phi_{T-XY}$ , respectively; in the transverse plane XZ, 0.02° and 0.1° for  $\phi_{R-XZ}$  and  $\phi_{T-XZ}$ , respectively, and in the sagittal plane ZY, 2.1° and 1.7° for  $\phi_{R-ZY}$  and  $\phi_{T-ZY}$ , respectively.

#### B. Angular Variation in Globular, $\mathcal{G}$ , Models

The eight deformed  $\mathcal{G}$  models, for C334 transmural distribution, exhibit varying QRS and T-wave angles with respect to the three VCG planes (Fig. 5, central columns), despite having a similar sphericity index. For each deformed model, we



**Fig. 5.** Depolarization and repolarization angles, plotted with a bias  $\Delta\theta$  or  $\Delta\phi$  reported on each column top, for visualization purposes. Each column corresponds to an angle and includes three subplots. The leftmost subplots include the angles estimate from  $\mathcal{C}$  case for the 15 different  $C_{uvw}$  transmural configurations, representing the central configurations (endo having 20%, 30%, and 40%) in dark green, with percentiles boxplot, and in light green otherwise except the reference C334 which is plotted in black square; the two extreme cases of C136 and C532, were surrounded by square and diamond, respectively. The middle plots have eight colored dots, corresponding to angles estimated from the  $\mathcal{G}_A$  to  $\mathcal{G}_H$  models deriving from the control  $\mathcal{C}$  at transmural distribution C334 (black square). The rightmost subplot includes angles estimates for  $\mathcal{G}_G$  (red) and  $\mathcal{G}_H$  (brown) for the extreme transmural configurations C136 (squares) and C532 (diamond).

computed the QRS and T-wave loops. Subsequently, we derived the average QRS loop and the average T-wave loop across all the deformed models. The average loops were then compared to the loops of each deformed model using a least squares adjustment. As a result the  $\mathcal{G}_C$  and  $\mathcal{G}_G$  models exhibited the closest similarity to the average QRS loop, while  $\mathcal{G}_G$  and  $\mathcal{G}_H$  demonstrated the closest similarity to the average T-wave loop. Based on this observation, the  $\mathcal{G}_G$  model was selected as the representative model. Additionally, considering that the  $\mathcal{G}_H$  model shares the same basal diameter deformation as the  $\mathcal{G}_G$  model but differs in terms of apex-base change, both the  $\mathcal{G}_G$  and  $\mathcal{G}_H$  models were chosen as the two representative deformed models in the study.

To analyze in detail the QRS loops changes, Fig. 6, we divided them into three colored segments: blue from loop start to 31 ms, gray from 31 to 64 ms, and magenta from 64 to 85 ms. We plotted the simulation results of the  $\mathcal{G}_G$  and  $\mathcal{G}_H$  models as representatives of average deformations.  $\mathcal{G}_G$  keeps an apex constraint as the reference point of deformation while  $\mathcal{G}_H$  keeps a base constraint.

In the first segment, the electrical propagation went from His bundle through the branches until the septum, discreetly to the right, as can be evidenced in the frontal plane of the VCG (Fig. 6).

Dominant vectors from  $\mathcal{G}_G$  and  $\mathcal{G}_H$  extended slightly towards the right side of the torso, probably due to the enlargement of the left ventricle in the upper third septal myocardium and there was a slightly angular change in the sagittal and transverse planes. In the second segment of the loop, between 31 and 64 ms (Fig. 6), the electrical propagation in the left ventricle predominated and the direction of the vector towards the lower left part of the torso can be observed. By decreasing the apex-base length in the  $\mathcal{G}$  models, the local activation time (LAT) of the region was reduced, causing a loop that reaches its maximum point faster. After the potentials reached the apex, propagation continued into the large regions corresponding to the free walls of the left ventricle. In the third segment of the loop, after 64 ms (Fig. 6), the last areas close to the base in the posterior area were mainly activated. In the globular  $\mathcal{G}$  models, the LAT was reduced on the base of the left and right ventricles.

Subsequently, three tests were performed on the  $\mathcal{G}_G$  model, incorporating transmural heterogeneities: C136, C334, and C532. The first and the last configurations were selected as extreme scenarios in the behavior of the T-wave, and the C334 was the one showing a behavior closer to the average, based on the tests carried out on the  $\mathcal{C}$  model, Fig. 4.

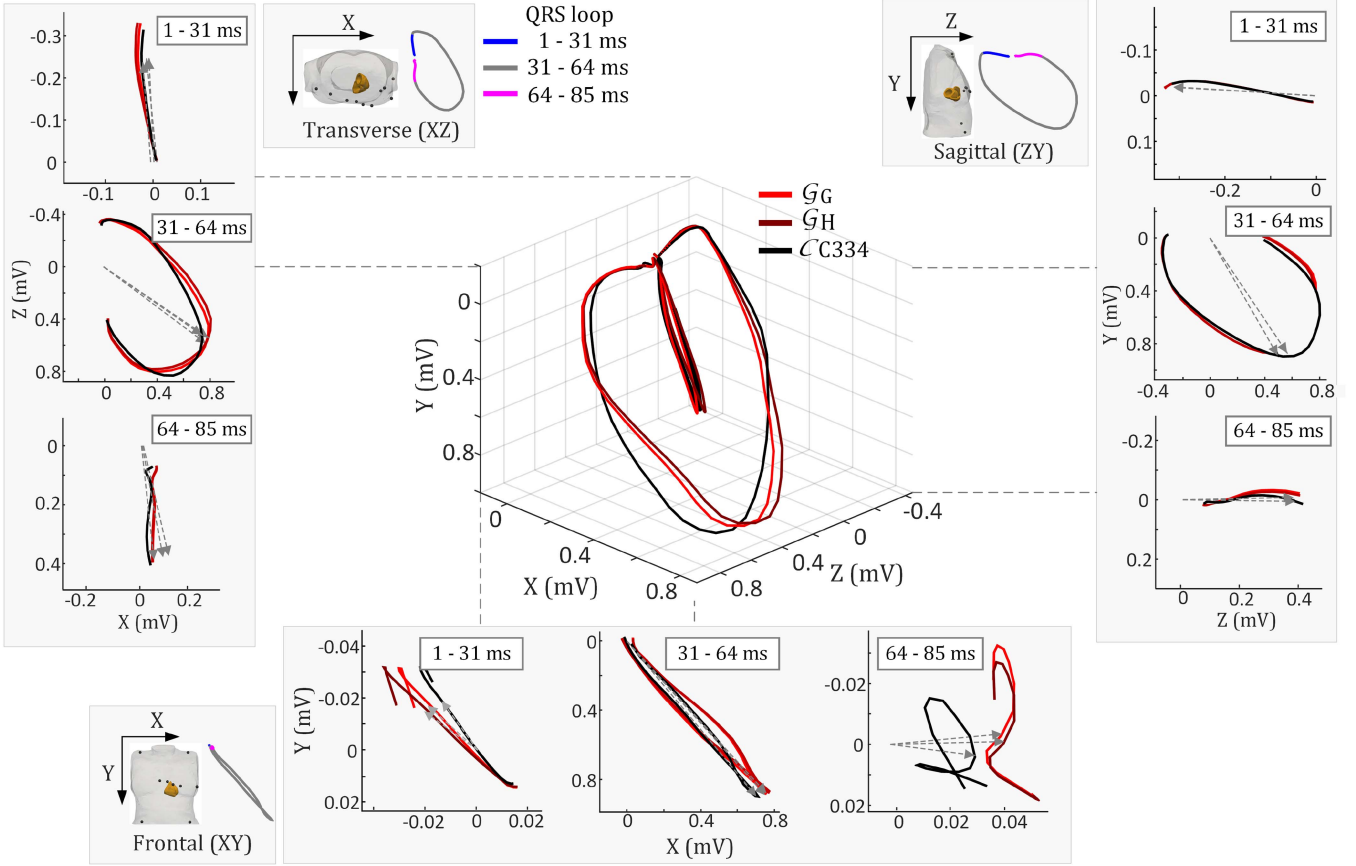


Fig. 6. Temporal segmentation of the QRS loop in three parts to analyze the vector changes. QRS loop projections of the  $\mathcal{C}$ , and its evolved  $\mathcal{G}_G$  and  $\mathcal{G}_H$  models, all in C334, between 1 and 31 ms, 31 and 64 ms, and 64 and 85 ms. Dashed arrows represent the dominant vectors of the loops.

TABLE II  
QRS AND T-WAVE ANGLES USING DIFFERENT TRANSMURAL HETEROGENEITIES ON  $\mathcal{G}_G$  MODEL

Angle (degrees)	C136			C334			C532		
	$\mathcal{C}$	$\mathcal{G}_G$	$\Delta \mathcal{R}$	$\mathcal{C}$	$\mathcal{G}_G$	$\Delta \mathcal{R}$	$\mathcal{C}$	$\mathcal{G}_G$	$\Delta \mathcal{R}$
$\phi_{R-XZ}$	43.1	<b>40.4</b>	-2.7 0.9	43.4	<b>40.2</b>	-3.1 0.9	43.2	<b>38.9</b>	-4.3 0.9
$\phi_{R-XY}$	22.6	<b>24.7</b>	2.1 1.1	24.2	<b>26.5</b>	2.3 1.1	29.0	<b>31.8</b>	2.8 1.1
$\phi_{R-ZY}$	38.4	<u>39.6</u>	1.2 1.0	36.9	<u>38.3</u>	1.4 1.0	33.0	<u>35.0</u>	2.0 1.1
$\phi_{T-XZ}$	37.1	<b>36.9</b>	-0.2 1.0	37.5	<b>37.1</b>	-0.4 1.0	38.0	<b>37.7</b>	-0.3 1.0
$\phi_{T-XY}$	30.5	<u>31.4</u>	0.9 1.0	28.7	<u>30.0</u>	1.2 1.0	22.4	<u>24.5</u>	2.1 1.1
$\phi_{T-ZY}$	37.9	<u>37.4</u>	-0.6 1.0	39.1	<u>38.4</u>	-0.7 1.0	43.6	<u>42.3</u>	-1.2 1.0
$\theta_{RT-XY}$	3.3	<b>0.8</b>	-2.5 0.2	4.9	<b>2.0</b>	-2.8 0.4	9.7	<b>5.3</b>	-4.4 0.5
$\phi_{R-XZ} - \phi_{T-XZ}$	6.0	<b>3.5</b>	-2.5 0.6	5.9	<b>3.1</b>	-2.8 0.5	5.2	<b>1.2</b>	-4.0 0.2
$\phi_{R-XY} - \phi_{T-XY}$	-7.9	<u>-6.8</u>	1.2 0.9	-4.5	<u>-3.5</u>	1.1 0.8	6.5	<b>7.2</b>	0.7 1.1
$\phi_{R-ZY} - \phi_{T-ZY}$	0.4	<b>2.2</b>	1.8 5.0	-2.2	<u>-0.2</u>	2.1 0.1	-10.6	<u>-7.3</u>	3.2 0.7

$\Delta$  and  $\mathcal{R}$ , angle difference and ratio, respectively, between deformed  $\mathcal{G}_G$  and control  $\mathcal{C}$  models. bold, and underlined, font highlights the angles which tendency of change between  $\mathcal{G}_G$  and  $\mathcal{C}$  models follows similar trend to clinical results between IUGR and control for preadolescents [8], and adults [9], respectively.

The C136 configuration reached a higher T-wave amplitude but decayed faster. On the contrary, C532 reached the lowest amplitude but extended its decay beyond the two additional compared models, Fig. 4. Regarding the QRS and T-wave angles, the C136 and C334 models maintained similar trends as those reported in the clinical data at certain angles ( $\theta_{RT-XY}$ ,  $\phi_{R-ZY}$ ,  $\phi_{T-XY}$ ,  $\phi_{T-ZY}$  for adults, and  $\theta_{RT-XY}$ ,  $\phi_{R-XZ}$ ,  $\phi_{R-XY}$ ,  $\phi_{T-XZ}$  for preadolescents, in Table II). To

compare the angular variation not only the angle difference values between control,  $\mathcal{C}$ , and deformation,  $\mathcal{G}$ , models,  $\Delta$ , were compared, but the relative change,  $\mathcal{R}$ , calculated as the ratio between angle at deformation  $\mathcal{G}$  and at control  $\mathcal{C}$ , was computed, and displayed in Table II. A value of  $\mathcal{R} < 1$  represents an angular reduction in the  $\mathcal{G}$  model with respect to the  $\mathcal{C}$  model and a value of  $\mathcal{R} > 1$  represents an increase. This index shows that the  $\theta_{RT-XY}$  angle decreases in the  $\mathcal{G}_G$



TABLE III

RESULTS ARE PRESENTED IN THREE BLOCKS: THE LEFTMOST BLOCK REPRESENTS THE CLINICAL DATA FOR PREADOLESCENTS, THE CENTRAL BLOCK REPRESENTS THE CLINICAL DATA FOR ADULTS, AND THE RIGHTMOST BLOCK REPRESENTS THE SIMULATION RESULTS

Angle (degrees)	Clinical result preadolescents [8]			Clinical result adults [9]			Simulations on C334				
	Control n = 60	IUGR n = 33	$\Delta \mathcal{R}$	Control n = 33	IUGR n = 54	$\Delta \mathcal{R}$	$\mathcal{C}$	$\mathcal{G}_G$	$\Delta \mathcal{R}$	$\mathcal{G}_H$	$\Delta \mathcal{R}$
$\phi_{R-XZ}$	37.6 (29.9 - 40.8)	34.2 (28.6 - 40.0)	-3.4 0.9	33.0 $\pm$ 9.1	35.7 $\pm$ 6.1	2.8 1.1	43.4	<b>40.2</b>	-3.1 0.9	<b>40.7</b>	-2.7 0.9
$\phi_{R-XY}$	20.0 (10.1 - 28.6)	25.5 (19.8 - 33.6)*	5.5 1.3	29.5 $\pm$ 13.0	22.1 $\pm$ 11.8**	-7.4 0.7	24.2	<b>26.5</b>	2.3 1.1	<b>24.5</b>	0.3 1.0
$\phi_{R-ZY}$	46.0 $\pm$ 9.3	43.1 $\pm$ 8.9	-2.9 0.9	40.7 $\pm$ 12.1	44.2 $\pm$ 9.8	3.5 1.1	36.9	<u>38.3</u>	1.4 1.0	<u>39.4</u>	2.5 1.1
$\phi_{T-XZ}$	36.4 (32.1 - 38.8)	32.0 (28.6 - 38.6)*	-4.4 0.9	29.4 $\pm$ 10.6	33.2 $\pm$ 10.7*	3.8 1.1	37.5	<b>37.1</b>	-0.4 1.0	<b>36.7</b>	-0.8 1.0
$\phi_{T-XY}$	29.4 (13.7 - 27.2)	21.5 (12.8 - 25.9)	-7.9 0.7	14.4 $\pm$ 8.7	14.5 $\pm$ 9.4	0.1 1.0	28.7	<u>30.0</u>	1.2 1.0	<b>28.0</b>	-0.7 1.0
$\phi_{T-ZY}$	47.2 (38.8 - 52.9)	47.9 (41.1 - 56.6)	0.7 1.0	54.8 $\pm$ 9.5	51.5 $\pm$ 12.1	-3.3 0.9	39.1	<u>38.4</u>	-0.7 1.0	<b>40.5</b>	1.4 1.0
$\theta_{RT-XY}$	6.6 (2.7 - 11.3)	6.5 (3.9 - 15.8)	-0.1 1.0	13.5 $\pm$ 13.7	9.3 $\pm$ 8.5**	-4.2 0.7	4.9	<u>2.0</u>	-2.8 0.4	<u>3.2</u>	-1.7 0.7
$\phi_{R-XZ} - \phi_{T-XZ}$	1.7 (-4.0 - 5.4)	0.9 (2.3 - 6.1)	-0.8 0.5	3.5 $\pm$ 9.6	2.5 $\pm$ 8.4	-0.9 0.7	5.9	<u>3.1</u>	-2.8 0.5	<b>4.0</b>	-1.9 0.7
$\phi_{R-XY} - \phi_{T-XY}$	-0.5 $\pm$ 14.1	5.3 $\pm$ 12.1*	5.8 -10.6	15.1 $\pm$ 14.1	7.6 $\pm$ 14.6**	-7.5 0.5	-4.5	<u>-3.5</u>	1.1 0.8	<u>-3.5</u>	1.0 0.8
$\phi_{R-ZY} - \phi_{T-ZY}$	-0.7 $\pm$ 12.5	-4.9 $\pm$ 12.7	-4.2 7.0	-14.1 $\pm$ 14.0	-7.4 $\pm$ 14.0**	6.8 0.5	-2.2	<u>-0.2</u>	2.1 0.1	<u>-1.1</u>	1.1 0.5

The loop angle values are reported as mean  $\pm$  standard deviation or interquartile range. Simulation results display the angles obtained or deformation  $\mathcal{G}_G$  and control  $\mathcal{C}$  in configuration C334. The angles that exhibit a tendency of change between  $\mathcal{G}_G$  and  $\mathcal{C}$  models, similar to the tendency observed between IUGR and control subjects for preadolescents [8], are highlighted in bold. Likewise, for adults [9], the angles are underlined. Significant differences \*p-value < 0.05, \*\*p-value < 0.01.

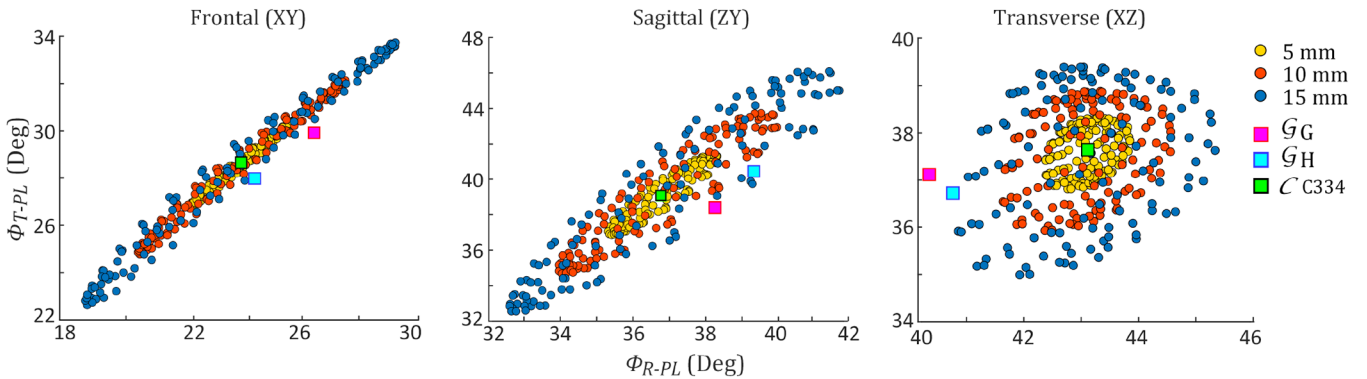


Fig. 7. QRS,  $\phi_{R-PL}$ , vs T-wave,  $\phi_{T-PL}$ , angles,  $PL \in \{XY, ZY, XZ\}$ , from the VCG, considering a 5 (yellow), 10 (orange), and 15 (blue) mm displacement of the heart inside the torso. Each color group shows one hundred and twenty tests. The green square shows the control  $\mathcal{C}$  results, and the magenta and cyan squares correspond to the angular results for the  $\mathcal{G}_G$  and  $\mathcal{G}_H$  models without displacement, respectively.

models compared to the  $\mathcal{C}$  model but in a non-homogeneous way. The  $\mathcal{R}$  index shows a noticeable change on  $\phi_{R-XZ} - \phi_{T-XZ}$ , less marked in  $\phi_{R-XY} - \phi_{T-XY}$ , and shows a pronounced heterogeneous change on the  $\phi_{R-ZY} - \phi_{T-ZY}$ . Here it is possible to observe that the models C136 and C532 generate opposite extreme angular values, Fig. 4. For further comparative testing we also report the C334 model results as the intermediate behaviour.

The  $\mathcal{G}$  models kept the same Purkinje network and the apico-basal gradient and transmural heterogeneities than the  $\mathcal{C}$  model. The angle measurements are presented in Table III. Second to fourth columns show the preadolescent results presented in [8], fifth to seventh columns show the adults results from [9], together with the  $\mathcal{R}$  and  $\Delta$  indexes. Results on  $\mathcal{G}_G$  and  $\mathcal{G}_H$  models relative to the  $\mathcal{C}$ , were shown from eighth to twelfth columns. Angles that followed in simulation the same trend as in the clinical data are highlighted in bold and underlined.

### C. Impact of Heart Position

The nodal displacement tests allowed us to identify the angular variation generated only by displacing the  $\mathcal{C}$  model a certain distance in different directions. Fig. 7 shows the values of the

QRS loop angles,  $\phi_{R-PL}$ , (horizontal axis) against the T-wave angles,  $\phi_{T-PL}$ , (vertical axis),  $PL \in \{XY, ZY, XZ\}$ . Simulations results without displacement are shown in big squares: green for the  $\mathcal{C}$  model (center of the clouds in Fig. 7 subplots) and magenta and cyan for the  $\mathcal{G}_G$  and  $\mathcal{G}_H$  models, respectively. Table IV presents the impact of heart displacement on the angular loops. The analysis shows that the maximum change in angle occurs in  $\phi_{T-ZY}$ , followed by  $\phi_{T-XY}$ . However, the relative angles (last three rows) exhibit lower changes, likely due to their nature as relative angles, where the influence of displacement is reduced. As observed earlier (Fig. 5), the transverse plane XZ showed lower angle variations. Based on Fig. 6, we observe that the deformations primarily occur along the X and Y axes, while the deformation along the Z axis is minimal. In addition, the loop in the XZ plane mainly spans along the Z axis, resulting in minimal changes to its axis. As a result, this contributes to the lower variability of angles observed in the XZ plane, even in the displacement tests.

The nodal displacement in all the  $\mathcal{G}_{A-H}$  models did not exceed 3 mm in all axes, for this reason, the angle measurements were compared against the 5 mm displacement in the Fig. 8. In this figure, the magenta region represents the angular variation obtained when the  $\mathcal{C}$  model is displaced 5 mm in any direction



**TABLE IV**  
ANGLE VALUE FOR MODEL  $\mathcal{C}$  WITH NO DISPLACEMENT, AND  $\pm$  STANDARD DEVIATION ( $\pm$ SD) WHEN  $\|\mathbf{d}_k\| \neq 0$

Control model $\mathcal{C}$ , with C334				
$\ \mathbf{d}_k\ $ (mm)	0	5	10	15
Degrees ( $^\circ$ )	Angle	SD	SD	SD
$\phi_{R-XZ}$	43.4	$\pm 0.5$	$\pm 0.9$	$\pm 1.4$
$\phi_{R-XY}$	24.2	$\pm 1.2$	$\pm 2.4$	$\pm 3.6$
$\phi_{R-ZY}$	36.9	$\pm 1.0$	$\pm 2.0$	$\pm 3.0$
$\phi_{T-XZ}$	37.5	$\pm 0.5$	$\pm 1.0$	$\pm 1.4$
$\phi_{T-XY}$	28.7	$\pm 1.2$	$\pm 2.5$	$\pm 3.8$
$\phi_{T-ZY}$	39.1	<b><math>\pm 1.5</math></b>	<b><math>\pm 3.0</math></b>	<b><math>\pm 4.6</math></b>
$\theta_{RT-XY}$	4.9	$\pm 0.7$	$\pm 1.5$	$\pm 2.2$
$\phi_{R-XZ} - \phi_{T-XZ}$	5.9	$\pm 0.6$	$\pm 1.2$	$\pm 1.8$
$\phi_{R-XY} - \phi_{T-XY}$	-4.5	$\pm 0.2$	$\pm 0.3$	$\pm 0.5$
$\phi_{R-ZY} - \phi_{T-ZY}$	-2.3	$\pm 0.7$	$\pm 1.4$	$\pm 2.0$

Bold font highlights the larger SD. Note that the angle value for  $\|\mathbf{d}_k\| \neq 0$  is the same as the mean angle for  $\|\mathbf{d}_k\| = 0$ .

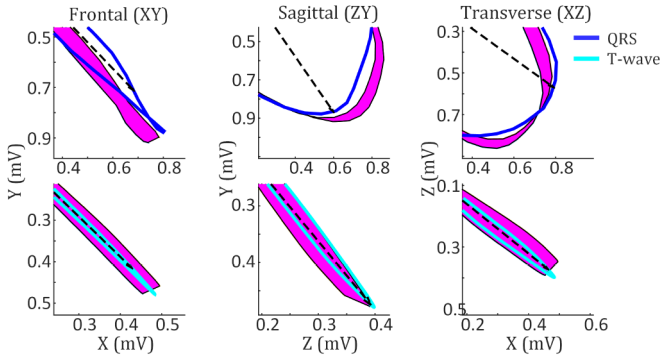


**Fig. 8.** QRS and T-wave loops in the three VCG planes. The magenta region corresponds to the angle variation when displacement  $\|\mathbf{d}_k\| = 5$  mm in any direction. QRS and T-wave loops correspond to the  $\mathcal{G}_G$  model simulation. Dotted lines represent the dominant vectors.

and is compared with the loop and dominant vector of the deformed  $\mathcal{G}_G$  model.

#### IV. DISCUSSION

Significant cardiac morphological changes as a consequence of IUGR remain from the fetal stage to adolescence and adulthood [4], [5], [9], [24] and have been associated with cardiovascular disease [1], [25], [26], [27]. The impact of morphological changes on cardiac electrical activity might contribute to a better understanding of IUGR-related cardiac remodeling. In this work, we evaluated whether the morphological changes described in IUGR subjects [5] result in the changes in QRS and T-wave loop angles observed in patients [8], [9], using computational models based on heart and torso realistic anatomies.

##### A. Angular Variability Analysis in Simulation

The incorporation of transmural heterogeneities to the control  $\mathcal{C}$  model aims to represent *in silico* the observed inter-patient variability in tissue proportions and assess its impact on the analyzed angular parameters. In Fig. 4, it is possible to see

the impact that transmural changes have on the amplitude of the T-wave and its duration, causing changes in all the angular parameters [28], but in different proportions. In Fig. 5, we can observe a higher dispersion of angles in the frontal plane XY. On the other hand, in the transverse plane XZ, the lowest variability in angles is evident for  $\phi_{R-XZ}$  and  $\phi_{T-XZ}$ .

IUGR can occur due to a combination of unfavourable maternal, placental, fetal, and genetic factors. Cardiac remodeling as a consequence of IUGR has been evidenced by a change in the ventricular sphericity index, reducing the apex-base length and increasing the basal diameter [5]. We deformed the  $\mathcal{C}$  model by applying loads on different regions of the ventricular model (Fig. 2). The simulated globular models underwent changes in their sphericity index that aligned with the magnitude observed in clinical data. These changes were achieved through the implementation of eight distinct deformation protocols, intended to replicate the effects of IUGR. The different methods applied to obtain the deformed models  $\mathcal{G}_{A-H}$  influence the angular parameters of the QRS and the T-wave. Fig. 5 shows these calculated angles, in addition to the reference angular value of the control  $\mathcal{C}$  model at configuration C334. QRS angles present greater variability than T-wave angles, because the reduction in the apex-base length and the widening of the basal diameter directly affect QRS, reducing the time in which the apex and the external walls of the left ventricle were activated.

In the simulation, a wide range of transmural differences were considered being C136 and C532 configurations the ones displaying extreme angular values. However, the angular variability resulting from transmural cell type is smaller than the one resulting from the deformations  $\mathcal{G}_{A-H}$  models in Fig. 5, particularly when only non extreme tissues dispersion is considered, consistent with the significant variations found in patients. Fig. 5 additionally shows the angular result when introducing extreme transmural heterogeneities (C136 and C532) on the deformed models  $\mathcal{G}_G$  and  $\mathcal{G}_H$ . As expected, this variation caused extreme angular values in the T-wave and minor changes in the QRS, following the same pattern of change evidenced in the results with the  $\mathcal{C}$  model.

The results obtained in this article were contrasted with clinical results of preadolescents [8] and adult subjects [9] with IUGR. Only some of the measured parameters present a statistically significant difference between IUGR and control subjects; however, they were not the same in preadolescents and adults, with the exception of:  $\phi_{R-XY}$ ,  $\phi_{T-XZ}$ , and  $\phi_{R-XY} - \phi_{T-XY}$ . Additionally, the intersubject angular variability is large resulting in apparent reverted mean trends between adolescence and adulthood. Despite this, the changes in depolarization and repolarization angles calculated *in silico* simulations were mostly concordant with the clinical results when evaluating the  $\mathcal{R}$  index, Table III.

These results support that the morphological remodelling of the heart is, at least partially, responsible for the observed electrophysiological changes modifying most of the depolarization and repolarization angles. However, angle variations were also observed to be sensitive to the relative position of the heart with respect to the torso and electrodes, although the impact of these variations were lower than those observed by the morphological

remodelling, for low displacements, as expected from electrode mispositioning, etc.

The  $\theta_{RT-XY}$  values, both in the  $\mathcal{C}$  and  $\mathcal{G}$  models, were within the ranges of healthy people [29]. A wider angle (greater than 100 degrees) is usually associated with changes in the T-wave axis rather than QRS related and carries a considerably increased cardiac risk [30]. Reasons for  $\theta_{RT}$  angle changes are associated to changes in ventricular repolarization itself, or secondary to conduction abnormalities [31], [32]. A wide spatial  $\theta_{RT}$  angle has been demonstrated to be a predictor of sudden cardiac death in the general population (low risk) and in groups considered to be at higher risk (clinical population) and a strong predictor of all-cause mortality in post-menopausal women [30], [32], [33]. In our study, the reduction in  $\theta_{RT-XY}$  can be attributed to changes in both the QRS and the T-wave dominant vectors, being the QRS angle the one showing the largest change (Table III). Both QRS and T-wave angles changed from control to deformed simulations without considering ventricular conduction abnormalities in the deformed model. A recent genome-wide association study showed that ventricular conduction abnormalities are the most likely cause of QRS-T angle widening, being able to counteract the reduction in  $\theta_{RT-XY}$  [31]. As far as we know, there have been no studies indicating that conduction abnormalities occur as a result of IUGR. Therefore, in this analysis, we have kept the same conduction system in the control and deformed models in order to specifically assess the effect of geometrical changes on the VCG loops.

This reduction in  $\theta_{RT-XY}$  between control and IUGR patients is tiny in the clinical results reported in [8] with  $\mathcal{R} = 1.0$ , and larger in [9] with  $\mathcal{R} = 0.7$ , and it is reproduced with a similar trend in the simulation results for the  $\mathcal{G}_G$  and  $\mathcal{G}_H$  models, with values of  $\mathcal{R} = 0.4$  and  $0.6$  respectively (Table III).

Regarding the transverse plane XZ, the clinical results show a significant difference only in  $\phi_{T-XZ}$ . The simulation results show a similar trend in adolescents and reverted in adults data ( $\mathcal{R} = 0.9$  for preadolescents,  $\mathcal{R} = 1.1$  for adults, and  $\mathcal{R} = 1.0$  for the  $\mathcal{G}_G$  and  $\mathcal{G}_H$  models). In the same plane,  $\phi_{R-XZ}$  shows an index  $\mathcal{R} = 0.9$  for the  $\mathcal{G}_G$  and  $\mathcal{G}_H$  models, similar to preadolescents and contrary to  $\mathcal{R} = 1.1$  in adults.

The angular variation with respect to the sagittal plane ZY does not show a significant difference in the clinical results; however, the  $\mathcal{R}$  index shows a trend similar to the simulations results. For  $\phi_{R-ZY}$ ,  $\mathcal{R} = 0.9$  (preadolescents),  $\mathcal{R} = 1.1$  (adults) and  $1.0$  for  $\mathcal{G}_G$  and  $1.1$  for  $\mathcal{G}_H$  model. For  $\phi_{T-ZY}$ ,  $\mathcal{R} = 1.0$  (preadolescents),  $\mathcal{R} = 0.9$  (adults) and  $1.0$  for  $\mathcal{G}_G$  and  $\mathcal{G}_H$  models.

The changes in planarity and roundness of the QRS and the T-wave loops in  $\mathcal{G}_G$  and  $\mathcal{G}_H$  models with respect to  $\mathcal{C}$  model were also computed as in [8], and did not evidence significant changes, similar to what was reported for clinical results in preadolescents [8]. Although the angular variations in QRS and the T-wave loops introduced by deformation were small, these variations were still greater than those generated by the incorporation of transmural heterogeneities or due to displacement of the heart alone. The angular variation is more accentuated ( $\mathcal{R}$  index more different from 1) when comparing the relative angular values between the QRS and the T-wave,  $\phi_{R-PL} - \phi_{T-PL}$ , last three rows in Table III, and its trend is congruent to the

clinical results in adults. Note that in preadolescents the angles at control were very small making the index  $\mathcal{R}$  less reliable.

## B. Analysis of the Angular Change Due to the Position of the Heart

We can see in Fig. 8 that, although the displacement of the  $\mathcal{G}_G$  model does not exceed 3 mm, the dominant vector direction of the QRS loop is clearly different, which supports the hypothesis that the angular variation is not only a result of the nodal displacement of the heart but also of its deformation.

In the 5 mm displacement test (Table IV), we found a linear angle variation with a maximum value of 1.5 degrees on T-wave loop with respect to the sagittal plane ZY. Considering the deformed models, the change in the  $\theta_{RT-XY}$  showed a variation of less than 3 degrees. This slight variation aligns with the clinical observations of IUGR preadolescents used for validation in this study, who showed an average change of 0.1 degrees [8]. Furthermore, IUGR adults displayed a mean change of 4.2 degrees [9]. These values for changes in the  $\theta_{RT-XY}$  angle are small compared to those produced by other clinical pathologies such as conduction abnormalities, suggesting that the IUGR preadolescents included in the study have not developed any conduction abnormality. Previous studies have shown that displacement of precordial leads by 2 cm can result in changes in R wave progression in the precordial zone [34].

Cardiac remodelling of the fetus involves various mechanisms inducing the morphological change, as an adaptation to pressure and volume excess and resulting in a reduction of the sphericity index. In addition to this anatomical remodelling, electrophysiological changes with dominant QRS and T-wave angular variations have been reported [8], [9]. *In silico* simulations have allowed us to observe that the anatomical variation of the sphericity index of the heart is associated with an angular modification of the depolarization and repolarization vectors on most of the angles, with a similar trend to that reported in the literature. The angles also result sensitive to the relative position of the ventricles with respect to the torso and to the electrodes placed on it, which introduces an additional factor to the sphericity in the interpretation of the results.

The globularly deformed  $\mathcal{G}$  model of the heart was based on the results presented by [5] where the change in the sphericity of preadolescents as a consequence of IUGR is evidenced with a subtle variation. Although the used sphericity index was obtained from a cohort of preadolescents, we still compare with adults based on the study in [6], where it is evidenced that anatomical and functional changes can be maintained from childhood to adulthood, even questioned by other studies [7]. Variations in the rotation of the heart within the torso were not considered in our deformed  $\mathcal{G}$  models, a factor that can alter the potentials calculated on the leads. This fact is strengthened by observing that the depolarization and repolarization angles and their tendency change significantly when the VCG is calculated using the coefficients for Kors regression transformation. We have included the results of VCG using the inverse Dower method to be able to contrast the results with those presented in the literature [8], [9].

The control  $\mathcal{C}$  and deformed  $\mathcal{G}$  models have been simulated keeping the same fiber orientation and the same Purkinje network adapted to the globular models in order to specifically assess the impact of the morphological changes on the depolarization and repolarization loop angles. The changes observed in the QRS angle are only due to the geometrical deformation as the conduction system remained unchanged in the control and the deformed models. Factors such as conduction abnormalities have not been taken into consideration and are deemed beyond the scope of this study, requiring proper remodeling quantification under IUGR to include the effects in a future study. Although it is known that intrauterine growth in an unfavorable environment leads to a different structuring of the fibers, which would change the cellular conductivity pattern [35], it has also been observed in adults that changes in pressure on an infarcted region do not lead to significant changes in fiber orientation at the edge of the infarct zone [7], which makes uncertain to what extent a change in pressure, characteristic of cardiac remodelling, leads to fiber orientation remodelling.

Future research should focus on extending the work presented here, using models of rounded hearts developed from real images and considering the position and rotation of the heart within the torso. Additionally, the impact of cardiac remodelling on the direction of the myocardial fibers and on the Purkinje network requires further studies.

## V. CONCLUSION

The findings of this computational study indicate that the sphericity index of the heart, which represents anatomical variations, partially accounts for the changes observed in the dominant vectors of depolarization and repolarization reported in clinical studies [8], [9]. Changes in the dominant depolarization and repolarization angles can result from both ventricular spherical alterations and the relative displacement of the heart in relation to the torso and attached electrodes. However, it has been observed that the angular variations caused solely by heart displacements are smaller than those generated by deformation, particularly when the displacement remains within a few mm.

The reduction in  $\theta_{RT-XY}$  and  $\theta_{R-XZ} - \theta_{T-XZ}$  aligns with the reported clinical trends in adults and preadolescents, highlighting them as suitable biomarkers for quantifying sphericity reduction. Furthermore, these relative measures focusing on the depolarization-repolarization relationship were less sensitive to changes in heart-to-electrode positioning, making them more robust and suitable for clinical use.

The variations observed in the absolute angles (i.e., the angles between depolarization and repolarization loops) in the computational simulations, as shown in the last three rows of Table III, do not align with the clinical data obtained from adults and/or preadolescents. This phenomenon can be attributed to the fact that the remodelling observed in preadolescents may not persist in adults [8], [9], thus affecting the comparison. Whether this is a result of methodological limitations or attenuation of the remodelling in adulthood will require future studies.

## REFERENCES

- [1] S. Visentin, F. Grumolato, G. B. Nardelli, B. Di Camillo, E. Grisan, and E. Cosmi, "Early origins of adult disease: Low birth weight and vascular remodeling," *Atherosclerosis*, vol. 237, no. 2, pp. 391–399, 2014, doi: [10.1016/j.atherosclerosis.2014.09.027](https://doi.org/10.1016/j.atherosclerosis.2014.09.027).
- [2] D. Sharma, S. Shastri, and P. Sharma, "Intrauterine growth restriction: Antenatal and postnatal aspects," *Clin. Med. Insights: Pediatrics*, vol. 10, 2016, Art. no. CMPed.S40070.
- [3] M. Cruz-Lemini et al., "Fetal cardiovascular remodeling persists at 6 months in infants with intrauterine growth restriction," *Ultrasound Obstet. Gynecol.*, vol. 48, no. 3, pp. 349–356, Sep. 2016, doi: [10.1002/uog.15767](https://doi.org/10.1002/uog.15767).
- [4] F. Crispi et al., "Fetal growth restriction results in remodeled and less efficient hearts in children," *Circulation*, vol. 121, no. 22, pp. 2427–2436, Jun. 2010, doi: [10.1161/CIRCULATIONAHA.110.937995](https://doi.org/10.1161/CIRCULATIONAHA.110.937995).
- [5] S. I. Sarvari et al., "Persistence of cardiac remodeling in preadolescents with fetal growth restriction," *Circulation: Cardiovasc. Imag.*, vol. 10, no. 1, Jan. 2017, Art. no. e005270, doi: [10.1161/CIRCIMAGING.116.005270](https://doi.org/10.1161/CIRCIMAGING.116.005270).
- [6] C. Arnott et al., "Subtle increases in heart size persist into adulthood in growth restricted babies: The cardiovascular risk in young finns study," *Open Heart*, vol. 2, no. 1, Aug. 2015, Art. no. e000265. [Online]. Available: <https://openheart.bmj.com/content/2/1/e000265>
- [7] J. C. Walker et al., "Helical myofiber orientation after myocardial infarction and left ventricular surgical restoration in sheep," *J. Thoracic Cardiovasc. Surg.*, vol. 129, no. 2, pp. 382–390, Feb. 2005.
- [8] N. Ortigosa et al., "Heart morphology differences induced by intrauterine growth restriction and preterm birth measured on the ECG at preadolescent age," *J. Electrocardiol.*, vol. 49, no. 3, pp. 401–409, 2016, doi: [10.1016/j.jelectrocard.2016.03.011](https://doi.org/10.1016/j.jelectrocard.2016.03.011).
- [9] N. Ortigosa et al., "Intrauterine growth restriction induced ECG morphological differences measured in adulthood," in *Proc. IEEE Comput. Cardiol.*, 2018, pp. 1–4.
- [10] M. J. Schlij et al., "Predicting ventricular arrhythmias in patients with ischemic heart disease: Clinical application of the ECG-derived QRS-T angle," *Circulation: Arrhythmia Electrophysiol.*, vol. 2, no. 5, pp. 548–554, Oct. 2009, doi: [10.1161/CIRCEP.109.859108](https://doi.org/10.1161/CIRCEP.109.859108).
- [11] F. L. Bueno-Palomeque et al., "Changes in QRS and T-wave loops subsequent to an increase in left ventricle globularity as in intrauterine growth restriction: A simulation study," in *Proc. IEEE Comput. Cardiol.*, 2020, pp. 1–4.
- [12] A. Mincholé, E. Zacur, R. Ariga, V. Grau, and B. Rodriguez, "MRI-based computational torso/biventricular multiscale models to investigate the impact of anatomical variability on the ECG QRS complex," *Front. Physiol.*, vol. 10, 2019, Art. no. 1103.
- [13] K. A. Mountris, C. Sanchez, and E. Pueyo, "A novel paradigm for in silico simulation of cardiac electrophysiology through the mixed collocation meshless Petrov-Galerkin method," in *Proc. IEEE Comput. Cardiol.*, 2019, pp. 1–4.
- [14] F. Sahli Costabal, D. E. Hurtado, and E. Kuhl, "Generating Purkinje networks in the human heart HHS Public Access," in *J. Biomech.*, vol. 49, no. 12, pp. 2455–2465, 2016.
- [15] P. Stewart, O. V. Aslanidi, D. Noble, P. J. Noble, M. R. Boyett, and H. Zhang, "Mathematical models of the electrical action potential of Purkinje fibre cells," *Philos. Trans. Roy. Soc. A: Math., Phys. Eng. Sci.*, vol. 367, no. 1896, pp. 2225–2255, 2009.
- [16] T. O'Hara, L. Virág, A. Varró, and Y. Rudy, "Simulation of the undiseased human cardiac ventricular action potential: Model formulation and experimental validation," *PLoS Comput. Biol.*, vol. 7, no. 5, May 2011, Art. no. e1002061.
- [17] R. Doste et al., "A rule-based method to model myocardial fiber orientation in cardiac biventricular geometries with outflow tracts," *Int. J. Numer. Methods Biomed. Eng.*, vol. 35, no. 4, Apr. 2019, Art. no. e3185.
- [18] D. D. Streeter, H. M. Spotnitz, D. P. Patel, J. Ross, and E. H. Sonnenblick, "Fiber orientation in the canine left ventricle during diastole and systole," *Circulation Res.*, vol. 24, no. 3, pp. 339–347, 1969. [Online]. Available: <https://www.ahajournals.org/doi/pdf/10.1161/01.RES.24.3.339>
- [19] E. Zacur et al., "MRI-Based heart and torso personalization for computer modeling and simulation of cardiac electrophysiology," in *Proc. Int. Workshop Bio-Imag. Visual. Patient-Customized Simul. Int. Workshop Point-of-Care Ultrasound*, 2017, pp. 61–70.
- [20] G. E. Dower, H. B. Machado, and J. A. Osborne, "On deriving the electrocardiogram from vectorcardiographic leads," *Clin. Cardiol.*, vol. 3, no. 2, pp. 87–95, 1980.

- [21] P. C. Viswanathan, R. M. Shaw, and Y. Rudy, "Effects of IKr and IKs heterogeneity on action potential duration and its rate dependence: A simulation study," *Circulation*, vol. 99, no. 18, pp. 2466–2474, May 1999. [Online]. Available: <https://pubmed.ncbi.nlm.nih.gov/10318671/>
- [22] S. A. Maas, B. J. Ellis, G. A. Ateshian, and J. A. Weiss, "FEBio: Finite elements for biomechanics," *J. Biomech. Eng.*, vol. 134, no. 1, 2012, Art. no. 011005.
- [23] B. Owen, N. Bojdo, A. Jivkov, B. Keavney, and A. Revell, "Structural modelling of the cardiovascular system," *Biomech. Model. Mechanobiol.*, vol. 17, no. 5, pp. 1217–1242, 2018.
- [24] F. Crispi et al., "Cardiac dysfunction and cell damage across clinical stages of severity in growth-restricted fetuses," *Amer. J. Obstet. Gynecol.*, vol. 199, no. 3, pp. 254.e1–254.e8, 2008. [Online]. Available: <https://pubmed.ncbi.nlm.nih.gov/18771973/>
- [25] L. Schirone et al., "A review of the molecular mechanisms underlying the development and progression of cardiac remodeling," *Oxidative Med. Cellular Longevity*, vol. 2017, 2017.
- [26] P. Ueda, S. Cnattingius, O. Stephansson, E. Ingelsson, J. F. Ludvigsson, and A. K. E. Bonamy, "Cerebrovascular and ischemic heart disease in young adults born preterm: A population-based Swedish cohort study," *Eur. J. Epidemiol.*, vol. 29, no. 4, pp. 253–260, Apr. 2014.
- [27] N. B. Ojeda, D. Grigore, and B. T. Alexander, "Intrauterine growth restriction: Fetal programming of hypertension and kidney disease," *Adv. Chronic Kidney Dis.*, vol. 15, no. 2, pp. 101–106, 2008.
- [28] H. A. Bukhari et al., "Transmural ventricular heterogeneities play a major role in determining T-wave morphology at different extracellular potassium levels," in *Proc. IEEE Comput. Cardiol.*, 2019, pp. 1–4.
- [29] P. W. MacFarlane, "The frontal plane QRS-T angle," *Europace*, vol. 14, no. 6, pp. 773–775, Jun. 2012. [Online]. Available: <https://pubmed.ncbi.nlm.nih.gov/22523378/>
- [30] A. L. Aro et al., "QRS-T angle as a predictor of sudden cardiac death in a middle-aged general population," *EP Europace*, vol. 14, no. 6, pp. 872–876, Jun. 2012. [Online]. Available: <https://academic.oup.com/europace/article/14/6/872/546697>
- [31] W. J. Young et al., "Genetic architecture of spatial electrical biomarkers for cardiac arrhythmia and relationship with cardiovascular disease," *Nature Commun.*, vol. 14, no. 1, 2023, Art. no. 1411.
- [32] A. Oehler, T. Feldman, C. A. Henrikson, and L. G. Tereshchenko, "QRS-T angle: A review," *Ann. Noninvasive Electrocardiol.*, vol. 19, no. 6, pp. 534–542, 2014.
- [33] I. Kardys, J. A. Kors, I. M. V. D. Meer, A. Hofman, D. A. M. V. D. Kuip, and J. C. M. Witteman, "Spatial QRS-T angle predicts cardiac death in a general population," 2003. [Online]. Available: <https://academic.oup.com/eurheartj/article/24/14/1357/501772>
- [34] M. V. Herman, D. A. Ingram, J. A. Levy, J. R. Cook, and R. J. Athans, "Variability of electrocardiographic precordial lead placement: A method to improve accuracy and reliability," *Clin. Cardiol.*, vol. 14, no. 6, pp. 469–476, Jun. 1991, doi: [10.1002/j.1932-8737.1991.tb00001.x](https://doi.org/10.1002/j.1932-8737.1991.tb00001.x).
- [35] F. Crispi, Á. Sepúlveda-Martínez, F. Crovetto, O. Gómez, B. Bijnens, and E. Gratacós, "Main patterns of fetal cardiac remodeling," *Fetal Diagn. Ther.*, vol. 47, pp. 337–344, 2020. [Online]. Available: [www.karger.com/ftd](http://www.karger.com/ftd)